Supplementary Information: Sub-millisecond Translational and Orientational Dynamics of a Freely Moving Single Nanoprobe

Joseph S. Beckwith and Haw Yang*

Department of Chemistry, Frick Laboratory, Princeton University, Princeton, New Jersey 08544, United States

E-mail: hawyang@princeton.edu

*To whom correspondence should be addressed

Contents

S1 Methods

S1.1 W Functions

The W functions in equation 1 are specified by [1]

$$W_1^{0^\circ}(\lambda) = \frac{1}{4}\{2(A+B)(3+H) - [A+3AH+4B(1+H)+4C(1+H)\cos 2\phi]\sin^2\theta + (1+3H)[B+C\cos 2\phi]\sin^4\theta\} \quad \text{(S1)}$$

$$W_{13}^{0^\circ}(\lambda) = \frac{1}{16}(1+3H)[B+C\cos 2\phi]\sin^2 2\theta \tag{S2}$$

$$W_{3}^{0^\circ}(\lambda) = \frac{1}{4}[2-2H+(1+3H)\sin^2\theta]\{A+[B+C\cos 2\phi]\sin^2\theta\} \tag{S3}$$

$$W_{1}^{90^\circ}(\lambda) = \frac{1}{4}\{2(A+B)(3+H)-[A+3AH+4B(1+H)-4C(1+H)\cos 2\phi]\sin^2\theta+(1+3H)[B-C\cos 2\phi]\sin^4\theta\} \tag{S4}$$

$$W_{13}^{90^\circ}(\lambda) = \frac{1}{16}(1+3H)[B-C\cos 2\phi]\sin^2 2\theta \tag{S5}$$

$$W_{3}^{90^\circ}(\lambda) = \frac{1}{4}[2-2H+(1+3H)\sin^2\theta]\{A+[B-C\cos 2\phi]\sin^2\theta\} \tag{S6}$$

$$W_{1}^{45^\circ}(\lambda) = \frac{1}{4}\{2(A+B)(3+H)-[A+3AH+4B(1+H)+4C(1+H)\sin 2\phi]\sin^2\theta+(1+3H)[B+C\sin 2\phi]\sin^4\theta\} \tag{S7}$$

$$W_{13}^{45^\circ}(\lambda) = \frac{1}{16}(1+3H)[B+C\sin 2\phi]\sin^2 2\theta \tag{S8}$$

$$W_{3}^{45^\circ}(\lambda) = \frac{1}{4}[2-2H+(1+3H)\sin^2\theta]\{A+[B+C\sin 2\phi]\sin^2\theta\} \tag{S9}$$

$$W_{1}^{135^\circ}(\lambda) = \frac{1}{4}\{2(A+B)(3+H)-[A+3AH+4B(1+H)-4C(1+H)\sin 2\phi]\sin^2\theta+(1+3H)[B-C\sin 2\phi]\sin^4\theta\} \tag{S10}$$

$$W_{13}^{135^\circ}(\lambda) = \frac{1}{16}(1+3H)[B-C\sin 2\phi]\sin^2 2\theta \tag{S11}$$

$$W_{3}^{135^\circ}(\lambda) = \frac{1}{4}[2-2H+(1+3H)\sin^2\theta]\{A+[B-C\sin 2\phi]\sin^2\theta\} \tag{S12}$$

The A, B, C, and H functions depend on the collection objective[2] and the condenser[3] respectively and they are described in Section S1.2.

S1.2 A, B, C, & H Functions

Unpolarised, annular illumination with wavelength λ and at an angle

$$\Theta(\lambda) = \sin^{-1}\left[\frac{\mathrm{NA_{cond}}}{n_{\mathrm{m}}(\lambda)}\right]$$

(where $\mathrm{NA_{cond}}$ and $n_{\mathrm{m}}(\lambda)$ are the numerical aperture of the condenser and the wavelength-dependent refractive index of the medium, respectively) impinges on a single, scattering particle which we assume to be either translationally stationary or freely moving in space but locked in the optical volume of a microscope.[4] The light scattered by the particle is collected over the solid angle bounded by

$$\Delta(\lambda) = \sin^{-1}\left[\frac{\mathrm{NA_{obj}}}{n_{\mathrm{m}}(\lambda)}\right]$$

where $\mathrm{NA_{obj}}$ is the numerical aperture of the collection objective and $n_{\mathrm{m}}(\lambda)$ is the wavelength-dependent refractive index of the medium as before. Both of these solid angles are shown in Fig. 1b.

The collection objective and condenser are further described by A, B and C terms (in the case of the collection objective) and an H term (in the case of the condenser) and these are defined, as in Fourkas[2] as:

$$A = \frac{1}{6} - \frac{1}{4}\cos\Delta + \frac{1}{12}\cos^3\Delta$$
$$B = \frac{1}{8}\cos\Delta - \frac{1}{8}\cos^3\Delta$$
$$C = \frac{7}{48} - \frac{1}{16}\cos\Delta - \frac{1}{16}\cos^2\Delta - \frac{1}{48}\cos^3\Delta$$

with the wavelength-dependence of these terms obviated for readability. The H term is defined as in Yang as:[3]

$$H = \cos 2\Theta.$$

S2 Real-Time 3D Single-Particle Tracking & Division-of-amplitude Polarimeter Instrumentation

S2.1 RT-3DSPT Module

The technique relies on an active feedback system that uses a 3D piezoelectric stage that compensates for the motion of a particle, locking the particle in the focus of the stationary microscope objective. This was achieved as follows. The scattering from unpolarized, halogen lamp, dark-field illumination (condenser NA 1.4, objective NA 0.7) was split in a 7:3 ratio (Sputter-coated, non-polarizing 30/70 Beamsplitter, *Chroma*). 70% was sent to the tracking optics. Two NIR filters (700 nm 25 mm Diameter, OD 4.0 Shortpass Filter, *Edmund Optics*) and one 630 nm cutoff filter (SCHOTT RG-630, 25.4 mm Diameter, *Edmund Optics*) were placed before the diffuser to provide only red illumination light here. 50% of the light sent to the tracking optics was projected using an optical cantilever of 2 m in length[5] onto two orthogonal prism mirrors. Each prism mirror, one for the X direction particle motion and the other for the Y particle direction, splits the signal onto two single photon counting avalanche photodiodes (APDs, *Perkin Elmer*, SPCM-AQRH-13). When a particle is centered in X or Y, the reading on the two corresponding APDs is equal. However, when $\sim$single nm deviations in the particle position occur, the detectors will have an imbalance in their signal that is used for feedback control, with the stage counteracting this motion to return the detectors to balance by moving the particle back to the center of the microscope focus. In this way, the X and Y motion is compensated for, "locking" the particle in the center of the focus in X and Y. To compensate for any motion in the Z (optical axis) direction, 50% of the light sent to the tracking optics was projected through a slightly axially offset pinhole (5 µm diameter here) which, when imaged onto an APD, provided a quasi-linear index into the deviation in Z when such an APD intensity was normalized against the four X-Y APDs. The signals from the APDs were transmitted to a field programmable gate array (FPGA, *National Instruments*, 7833R) which applied an auto-regressive filter of

$$Y(n) = Y(n-1) + 0.003[X(n) - Y(n-1)]$$

where n is the signal index and X and Y refer to the unfiltered and filtered signals, respectively.[6] These filtered signals were then used to construct feedback signals using a proportional-integral (PI) controller. These feedback signals were then sent, at a rate of 100 kHz, to the piezoelectric stage (*Physik Instrumente*, P-561.3DD) to keep the particle at the center of the focal volume.

The piezoelectric stage used here had a translation range of 45 µm×45 µm×15 µm. It is not expected that changes in rod orientation should affect the single-particle tracking localization precision as whilst the PSF intensity distributions have been shown to be orientation dependent by Enderlein *et al.*[7] they found that the position error was dependent on objective numerical aperture. They specifically found that at an NA of 1.2 the position error would only be < 2.5 nm. As we here use an NA of 0.7 it can be anticipated that position error due to this effect is minimal.

S2.2 Division-of-amplitude polarimeter

The division-of-amplitude polarimeter consists of four APDs (*Perkin Elmer*, SPCM-AQRH-13) to measure the intensities at the polarization angles of 0°, 45°, 90°, and 135°. 30% of the light from the initial beamsplitter was sent to the orientation module, after which it was further split in a 1:1 ratio (Silver sputtered non-polarizing 50/50 Vis Beamsplitter, *Chroma*). Light transmitted by this beamsplitter was then sent into a polarizing beamsplitter (*Newport*, 05FC16PB.3) after which the transmitted light from this was focused onto the 90° detection APD. The reflected light was passed through a Glan-Taylor polarizer (350–700 nm AR Coating, *Thorlabs*) for polarization cleanup and then was focused onto the 0° detection APD. Light reflected by the 1:1 beamsplitter was sent into a Wollaston Prism (20° Beam Separation, 350–700 nm AR-Coated Calcite, *Thorlabs*) set at a 45° angle and the two separate beams focused into the 45° and 135° detection APDs. Note well that the choice of beamsplitters can make a significant impact in the division-of-amplitude-polarimeter's performance, with attempts at using cube beamsplitters and pellicle beamsplitters both finding significant deviations from desired polarization extinction ratios. We highly recommend characterizing the response of individual beamsplitters to polarized illumination by the use of a linear polarizer and a half-wave plate before their use in such a technique.

S3 Division-of-amplitude polarimeter characterization

Before analysis, it is necessary to treat the experimental data with an experimental correction factor in order to perform a more accurate comparison with theory. To do this, the division-of-amplitude polarimeter was characterized in the following manner. We passed unpolarized light through a linear polarizer and then directed this polarized light through the collection objective and rotated the polarization with a half-wave plate. This resulted in the data shown in Fig. S1.

These data were modeled using a function of the form

$$f(x) = A\cos(2x - B) + C$$

with the intensity weight at a single detector being $B_{n^\circ} + C_{n^\circ}$, and the average intensity weight being a mean of these four values ($I\bar{W}$). From this we may derive a multiplication factor with which each measured detector's photon counts can be multiplied by to compensate for imbalances in how efficiently each channel collected photons. The correction factors for the detectors are

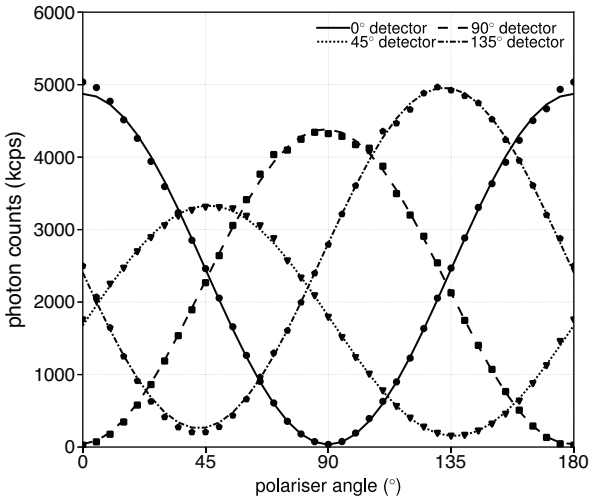

Figure S1: Counts measured at each detector as a function of incident light polarization.

$$\mathbf{CF} = \begin{pmatrix} I\bar{W}/(B_{0^\circ} + C_{0^\circ}) \\ I\bar{W}/(B_{45^\circ} + C_{45^\circ}) \\ I\bar{W}/(B_{90^\circ} + C_{90^\circ}) \\ I\bar{W}/(B_{135^\circ} + C_{135^\circ}) \end{pmatrix}$$

and before analysis the raw photon counts were multiplied by this factor.

The fits to the data in Fig. S1 also enable us to correct for the finite extinction ratios of the polarization optics, as the theoretical treatment underlying the theory assumes the collection optics are polarization preserving.[2] Thus we correct for this in our analysis by adding the extinction ratio values to our simulated data in our comparison algorithm.

We do not characterize any possible lamp polarization bias, as we have assumed that based on previous work where minor changes in polarization contrast fluctuations were measured and related to particle geometry,[1] if such an effect of polarization in the lamp source is present the effect on results is minor.

S4 Sample Preparation

S4.1 Static Nanoparticle Experiments

For experiments in which we compare our orientation determination performance to the shot noise limit, we suspend 92 nm×40 nm gold nanorods (AuNRs, Gold Nanorodz, A12-40-700-CIT-DIH-1-25, Lot #K8327, *Nanopartz*) in and 8% polyacrylamide gel,[8] chosen due to its similar refractive index to water and high optical clarity. We utilized the same preparation as Bryon and Variano,[8] scaled down by a factor of 10 and with 12.5% by volume of the AuNR solution added to the gel preparation. 16.5 µL of this was then sealed between a glass slide (12-544-12, *Fisher Scientific*) and a smaller glass coverslip (12-548-A, *Fisher Scientific*) using an adhesive spacer (S24735, *Molecular Probes*) and left to dry for ∼3 h, giving a sample depth of ≈120 µm. These were then imaged

using the microscope, with each rod being "tracked" for at least 10 s before scanning for further rods.

S4.2 Freely Diffusing Nanoparticle Experiments

For experiments in which we simultaneously track freely-diffusing nanoparticles while determining their 3D, orientation the sample consisted of 1 µL AuNRs (same AuNRs as Section S4.1) and 99 µL stock solution of 61:39 v:v glycerol:H_2O. The H_2O was milli-Q purity and the glycerol was from Fisher (G33-1, Lot 167117, *Fisher Chemical*) and used as received. As above, 16.5 µL of this was sealed between slide and cover slip using a spacer. Centering this sample at 60 µm above the lower slide ensured an isotropic environment for the tracked particle, due to the 15 µm Z travel range of the piezoelectric stage.

S4.3 TEM

Transmission electron microscopy (TEM) measurements were taken with a Philips CM-100 at 130,000x magnification and with an accelerating voltage of 80 kV. For the sample, 5 µL of the stock AuNRs were pipetted onto a TEM grid (CF400-CU-UL, *Electron Microscopy Sciences*) and incubated at room temperature for 15 minutes. Measurements were taken after wicking away any excess fluid with filter paper and air drying. The images of the particles were converted to binary images using Otsu's method and their lengths and widths taken as length and width of the bounding box of the particle areas.

S5 Numerical Simulation

For simulating experimental data, we must combine multiple things. We must simulate rotational diffusion to generate the underlying coordinates, and we must then assign photons to each detectors based on this. This procedure is described in the following sections. Here we simulate a random walk of 2×10^6 2 µs time steps and a D_R of 2504.08 rad^2s^{-1}. This value was chosen to represent an 80 nm diameter sphere in water, and was chosen to simplify simulation (due to this giving 0.1 rad distribution widths, see below). This rotational diffusion coefficient is, NB, much higher than the $\sim$200 rad^2s^{-1} D_R expected in experiment.

S5.0.1 Langevin Dynamics of Rotation

From Hunter *et al.*,[9] we may simluate a random walk of rotational motion by selecting three random angles a, b and c from a Gaussian distribution with a standard deviation of $(2\bar{D}_R)^{1/2}$. $\bar{D}_R$ is defined as

$$\bar{D}_R = D_R \tau_s \tag{S14}$$

and represents a dimensionless rotational diffusion coefficient defined in relation to the time duration of a single step (τ_s). For a particle of 80 nm in diameter in water, sampled every 2 µs, this value is 0.1 rad. This distribution ensures that the simulated dynamics will be in agreement with the Stokes-Einstein-Debye relation, and where the theoretical rotational diffusion coefficient may be calculated using

$$D_R = \frac{k_B T}{\pi \eta d^3} \tag{S15}$$

where k_B is Boltmann's constant, T is the temperature, η is the viscosity of the surrounding medium, and d is the effective hydrodynamic diameter of the particle. The particle (or, the vector(s) we are using to describe the polarisation of the particle) is rotated by an angle c about the Z-axis, then by an angle b about the Y-axis, then finally by an angle a about the X-axis to produce the particle at a subsequent time. The rotation matrices used are:

$$\mathbf{R}_X(a) = \begin{pmatrix} 1 & 0 & 0 \\ 0 & \cos a & -\sin a \\ 0 & \sin a & \cos a \end{pmatrix} \tag{S16a}$$

$$\mathbf{R}_Y(b) = \begin{pmatrix} \cos b & 0 & \sin b \\ 0 & 1 & 0 \\ -\sin b & 0 & \cos b \end{pmatrix} \tag{S16b}$$

$$\mathbf{R}_Z(c) = \begin{pmatrix} \cos c & -\sin c & 0 \\ \sin c & \cos c & 0 \\ 0 & 0 & 1 \end{pmatrix} \tag{S16c}$$

after which, given an initial unit position vector $\mathbf{x^0}$, the subsequent position vector is:

$$\mathbf{x} = \mathbf{R}_X \mathbf{R}_Y \mathbf{R}_Z \mathbf{x^0} \tag{S17}$$

thus we may simulate our particle rotation. We may convert our Cartesian coordinates to the spherical coordinates that we will use later in scattering calculations using:

$$\theta = \cos^{-1}\left(\frac{Z}{\sqrt{X^2+Y^2+Z^2}}\right) \tag{S18a}$$

$$\phi = \arctan 2(Y,X) \backslash 2\pi \tag{S18b}$$

where the $\backslash$ in the equation for the ϕ reflects that one takes the remainder from the division of $\arctan 2(Y,X)/2\pi$. By convention the range of angles that θ may explore is 0 to π, and ϕ may explore 0 to 2π. As the analysis method used here is symmetric about $\pi/2$ in θ and π in ϕ, these angles are then transformed by

$$\theta > \pi/2 = |(\theta > \pi/2) - \pi| \tag{S19a}$$

$$\phi > \pi = |(\phi > \pi) - \pi|. \tag{S19b}$$

S5.0.2 Making a Stochastic Photon Stream

At each step of the rotational random walk described above, we must generate how many photons we expect to see from our particle at time step j the specified θ_j with its intensity dependent on equation

$$\begin{aligned}\mathrm{NF_s} = \Big(&2(A+B)(3+H)- \\ &(A+3AH+4B(1+H))\sin^2(\theta)+B(1+3H)\sin^4(\theta)\Big)\alpha_1 \\ &+B(1+3H)\cos^2(\theta)\sin^2(\theta)\alpha_{13} \\ &-\frac{1}{4}(2A+B-B\cos(2\theta))(-5+H+(1+3H)\cos(2\theta))\alpha_3 \end{aligned} \quad \text{(S20)}$$

where

$$\alpha_1(\lambda) = w|\alpha_1|^2,$$

$$\alpha_{13}(\lambda) = w(\alpha_1\bar{\alpha}_3 + \bar{\alpha}_1\alpha_3)$$

and

$$\alpha_3(\lambda) = w|\alpha_3|^2$$

with the A, B, C and H terms defined as in Section S1.2.

First, at each time step t we draw inter-photon durations Δ_t from an exponential probability distribution [10]

$$f(\Delta_t; I_j) = I_j \mathrm{e}^{-I_j\Delta_t} \quad \text{(S21)}$$

where the subscript j refers to the intensity state of time point j and is computed by multiplying equation S20 with the appropriate instrument-dependent functions, θ_j, α_1, α_{13} and α_3 with the specified average intensity I. We continue to draw photons until the total of the inter-photon durations is above the bin time, then discard one. These photons are then assigned to wavelengths. If we are illuminating with multiple wavelengths (i.e., with a lamp) then at each jth step of our random walk we must stochastically assign our N_p photons. Here we take our lamp spectrum to be that of the detector-weighted illumination intensity of a halogen lamp present in our laboratory with a 630 nm cutoff filter (SCHOTT RG-630, 25.4 mm Diameter, *Edmund Optics*) and two NIR filters (700 nm 25 mm Diameter, OD 4.0 Shortpass Filter, *Edmund Optics*) added. This spectrum is shown in Fig. S2.

We may assign a wavelength to each kth photon p_k, $\lambda(p_k) \to \lambda_i$, in the jth step by finding the wavelength index i such that the bracketing values q_{i-1} and q_i have r_k fall between them, i.e., $q_{i-1} \leq r_k < q_i$. r_k is randomly sampled from a normal distribution. The qs are defined as: $q_0 = -q_{N_\lambda} = -\infty$,

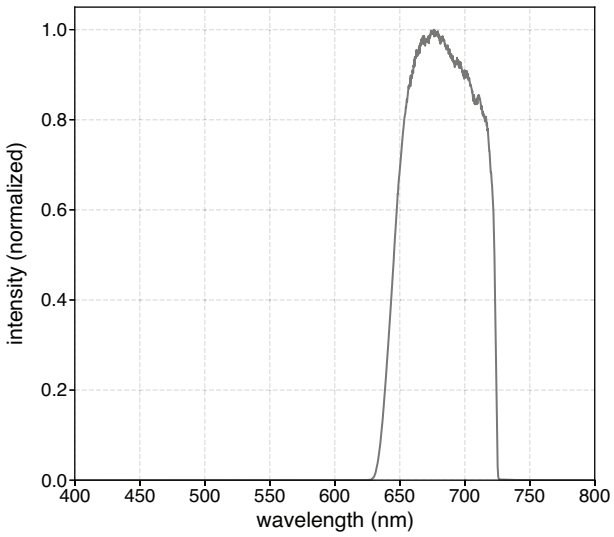

Figure S2: Experimental lamp spectrum.

$$q_{i-1} = -\sqrt{2}\text{erfc}^{-1}\left\{\frac{2\sum_{n=1}^{i-1}[\sum_{pol} I^*_{pol}(\theta_j,\phi_j,\lambda_n,S)]}{\sum_{n=1}^{N_\lambda}[\sum_{pol} I^*_{pol}(\theta_j,\phi_j,\lambda_n,S)]}\right\}, \tag{S22a}$$

$$q_i = -\sqrt{2}\text{erfc}^{-1}\left\{\frac{2\sum_{n=1}^{i}[\sum_{pol} I^*_{pol}(\theta_j,\phi_j,\lambda_n,S)]}{\sum_{n=1}^{N_\lambda}[\sum_{pol} I^*_{pol}(\theta_j,\phi_j,\lambda_n,S)]}\right\}, \tag{S22b}$$

where $\sum_{pol}$ represents a sum over any and all polarization components present in the experimental geometry, and the asterisks denote normalization of the intensities by I_j and S.[11] Next all of the photons in the jth step are individually assigned a polarization. This is accomplished by drawing a random number s_k from a random uniform distribution in the interval (0,1), and then assigning the polarization based on normalizing the with respect to their sum and placing the photon in the 'bin' defined by that normalization. Thus, if we have four polarizations, photon p_k will end up as 0°, 45°, 90° or 135° under the conditions:

$$p_k \in 0^\circ \quad \text{if} \quad s_k < \frac{I^*_{0^\circ}}{\sum_{pol} I^*_{pol}} \tag{S23a}$$

$$p_k \in 45^\circ \quad \text{if} \quad \frac{I^*_{0^\circ}}{\sum_{pol} I^*_{pol}} \leq s_k < \frac{I^*_{0^\circ} + I^*_{45^\circ}}{\sum_{pol} I^*_{pol}} \tag{S23b}$$

$$p_k \in 90^\circ \quad \text{if} \quad \frac{I^*_{0^\circ} + I^*_{45^\circ}}{\sum_{pol} I^*_{pol}} \leq s_k < \frac{I^*_{0^\circ} + I^*_{45^\circ} + I^*_{90^\circ}}{\sum_{pol} I^*_{pol}} \tag{S23c}$$

$$p_k \in 135^\circ \quad \text{if} \quad \frac{I^*_{0^\circ} + I^*_{45^\circ} + I^*_{90^\circ}}{\sum_{pol} I^*_{pol}} \leq s_k \leq \frac{\sum_{pol} I^*_{pol}}{\sum_{pol} I^*_{pol}} \tag{S23d}$$

where the $(\theta_j,\phi_j,\lambda_n,S)$ of I_{pol} has been removed for clarity. For most accurate comparison with real experimental conditions, these probabilities were altered in two ways with respect to ideal conditions.

First, they had a minimum value added at all angles that reflected the maximum extinction ratio possible with the polarizers

used in the real experiment. Then, each probability was multiplied by a weighting factor reflecting how each detector more or less efficiently collected photons in the real experiment (with the weighting factors averaging to 1). These correction factors are discussed in relation to their application to real experimental data in Section S3.

S6 Data Analysis

In order to most accurately deduce the 3D orientation of a AuNR, use detailed numerical simulations of our experiment (Section S5) to determine what the most accurate data analysis method is at different photon flux levels. We thus use this simulator to analyze two different analysis strategies. One is common to both angles with a one specific to θ. In the case of both ϕ and θ, we tested minimizing the squared error of the measured intensities at all detectors $\vec{I}$ versus the predicted intensities $f(\vec{I})$

$$\min_{\phi,\theta} ||\vec{I} - f(\vec{I})||_2^2$$

which we refer to as ratio & intensity optimization. We also tested minimizing the squared error of the measured ratio between the four detectors $\vec{I}/\max(\vec{I})$ versus the predicted ratio $f(\vec{I})/\max(f(\vec{I}))$

$$\min_{\phi,\theta} ||\vec{I}/\max(\vec{I}) - f(\vec{I})/\max(f(\vec{I}))||_2^2$$

which we refer to as ratio optimization. We also tested a separate analysis for θ, minimizing the squared error of the measured sum intensity from all detectors versus the predicted intensity from equation S20

$$\min_{\theta} ||\sum_k I_{s,k} - f(\sum_k I_{s,k})||_2^2$$

which we refer to as intensity optimization. In order to reduce a previously-determined problem with analyzing these data,[12] we applied a moving-average filter of differing bin number n_{avg} to the raw data before analysis, then averaged n_{avg} of these values to convert back to the initial time axis. This was only applied in the case of analysis to extract the θ parameter (as it severely compromised the ϕ histograms extracted, data not shown) and this θ was then used to determine ϕ using the raw data. For the data presented in Fig. 3, an n_{avg} of 1 was used. A comparison between these various data analysis methods is presented in Fig. S3.

It is clear from inspection of the upper panel of Fig. S3 that the optimal data analysis strategy, with no background photons present, for deducing θ values from experimental data is dependent on photon flux. For low photon flux, the best is that of the intensity & ratio optimization, followed by the intensity optimization, followed by ratio optimization. At high photon flux, the reverse is true—ratio optimization is superior. In addition, the benefit of the moving-average filter is lost at higher photon counts, such that at high photon flux no averaging seems the best strategy. Where ergodicity cannot be assumed and thus predicted intensities cannot be known, ratio optimization is the best choice.

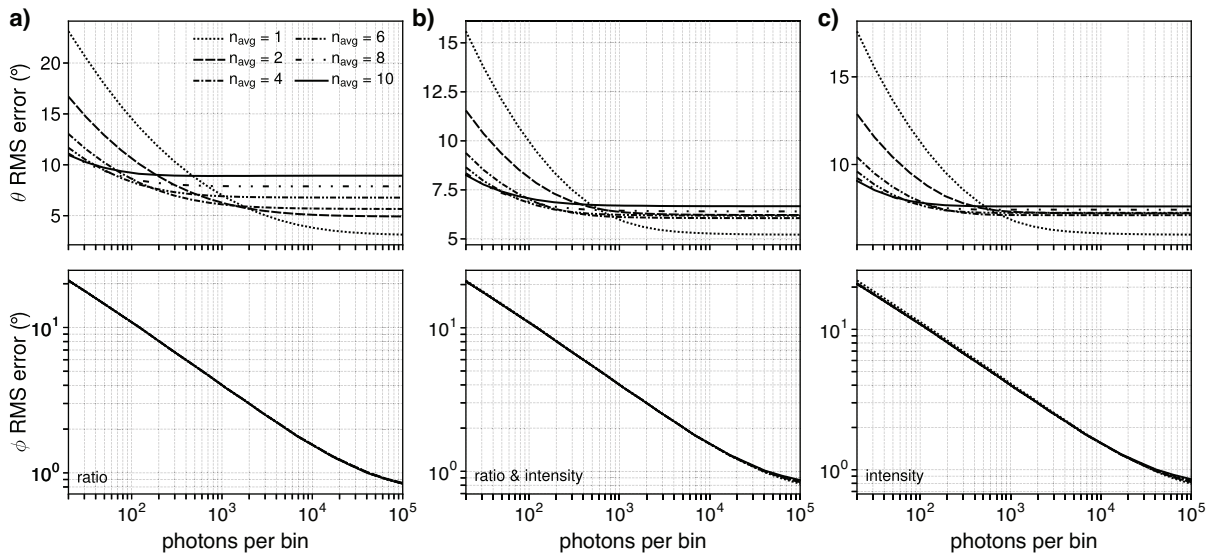

Figure S3: A comparison between various data analysis methods' accuracy in deducing θ (top) and ϕ (bottom) at various numbers of photons per bin and n_{avg}. Rods illuminated by a lamp spectrum shown in Fig. S2. a) Shows the ratio optimization strategy, b) shows the ratio & intensity optimization strategy, c) shows the intensity optimization strategy.

S7 Static Rods

In the case of a static rod, the intensities at each channel should be a Poisson distribution and an autocorrelation of the detector intensity fluctuation should give totally uncorrelated noise. Whilst we do observe some correlation, as defined by the test of Hanson and Yang,[13] in the case of our embedded AuNRs it appears to be substantially less than in the case of freely rotating rods, as shown in Fig. S4. Indeed, the correlation observed here appears close to two orders of magnitude less than in the case of freely rotating rods and the counts per detector appear very well approximated by Poisson distributions (example shown in Fig. S5). In addition, the AuNRs appear translationally static, with X, Y, and Z positions centered around 0 (shown in Fig. S7). We thus take these rods to be approximately static rotationally, suitable for analysis. To further ensure this, any rod that was found to have an initial autocorrelation function value of above 0.1, which is approximately an order-of-magnitude below the average initial autocorrelation value of freely diffusing rods, was not analyzed. Distributions of the initial autocorrelation function values are shown in Fig. S6. In addition, any rods that were oriented at $\theta = 90^{\circ}$ were excluded from the analysis, as these rods exhibit extremely small measurement uncertainties due to the issue with the data anlysis techniques discussed in the text and previously discussed by Lu and Vanden Bout.[12]

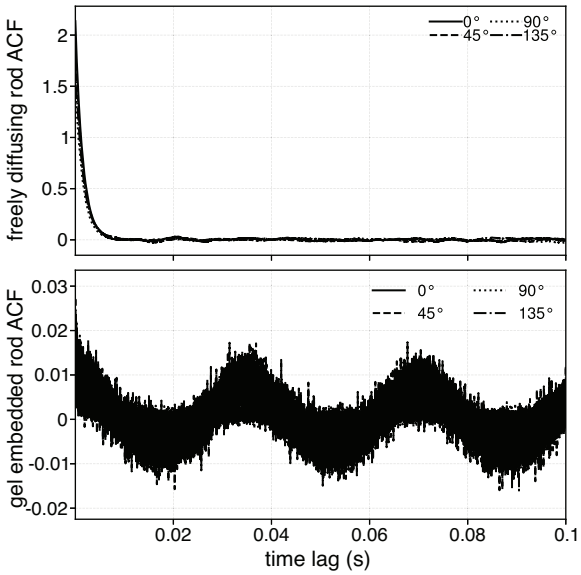

Figure S4: Autocorrelation of polarization detectors of a) freely diffusing AuNR and b) AuNR embedded in polyacrylamide. As can be seen, the initial amplitude of the freely diffusing AuNRs is considerably higher.

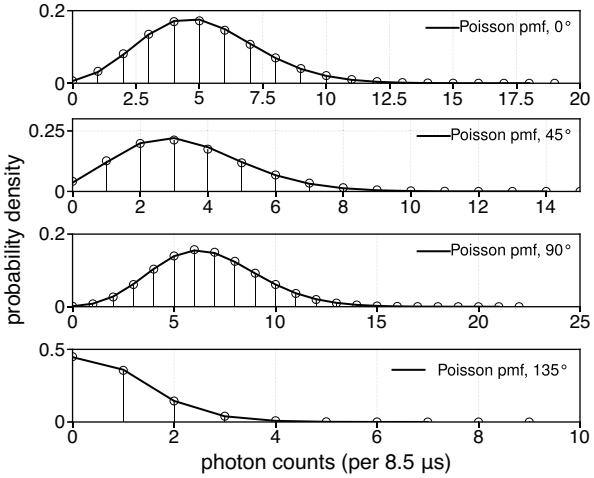

Figure S5: Poisson distribution fit to the counts detected at each polarization detector for an AuNR embedded in polyacrylamide. The Poisson distribution appears to describe the data reasonably well, which is not the case for the freely diffusing AuNRs.

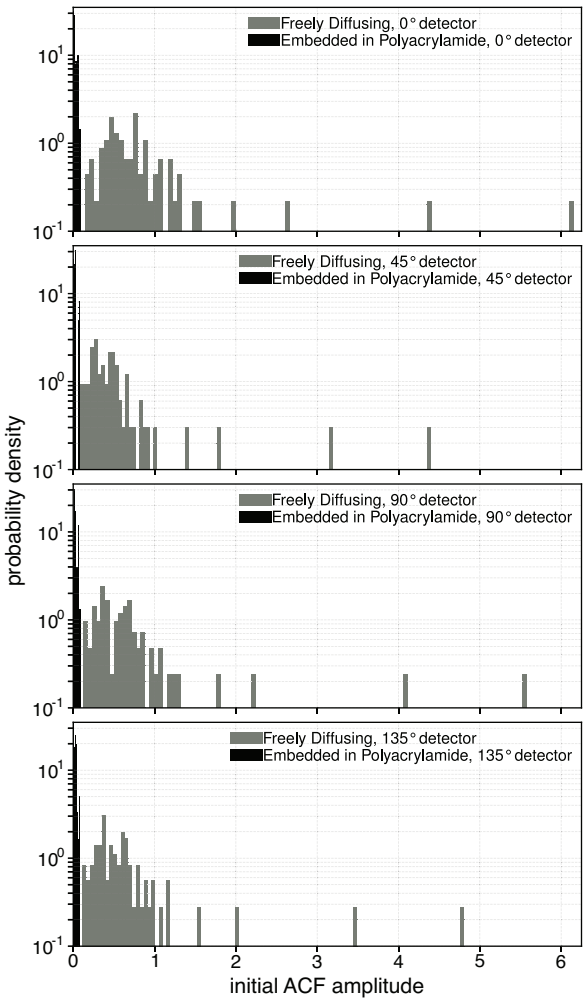

Figure S6: A comparison of the initial values of the autocorrelation functions of the polarization detector channels in the case of rods embedded in polyacrylamide (black) and in nominally 40/60 v/v glycerol/water (grey).

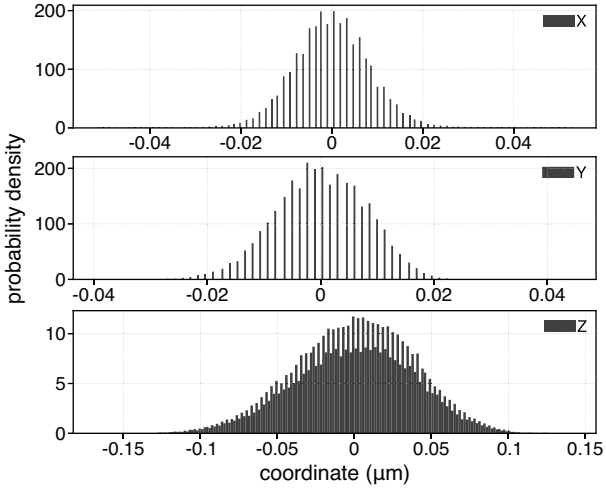

Figure S7: Location of AuNR in polyacrylamide as reported by the 3D-SPT over a 60 s track. As can be seen, the position reported does not appear to substantially move beyond the error in the tracking.

S8 Translational Diffusion Coefficients

For analysis of tracking trajectories, three-dimensional diffusion coefficients were calculated from the underlying 1D diffusion coefficients. These were calculated using the maximum likelihood estimator (MLE) constructed by Montiel *et al.* [14] correcting for the auto-regressive filter applied to the photon counts using the formula of Xu *et al.* [6] We also apply the focal-shift correction of Guerra *et al.* [1] to the Z-displacements.

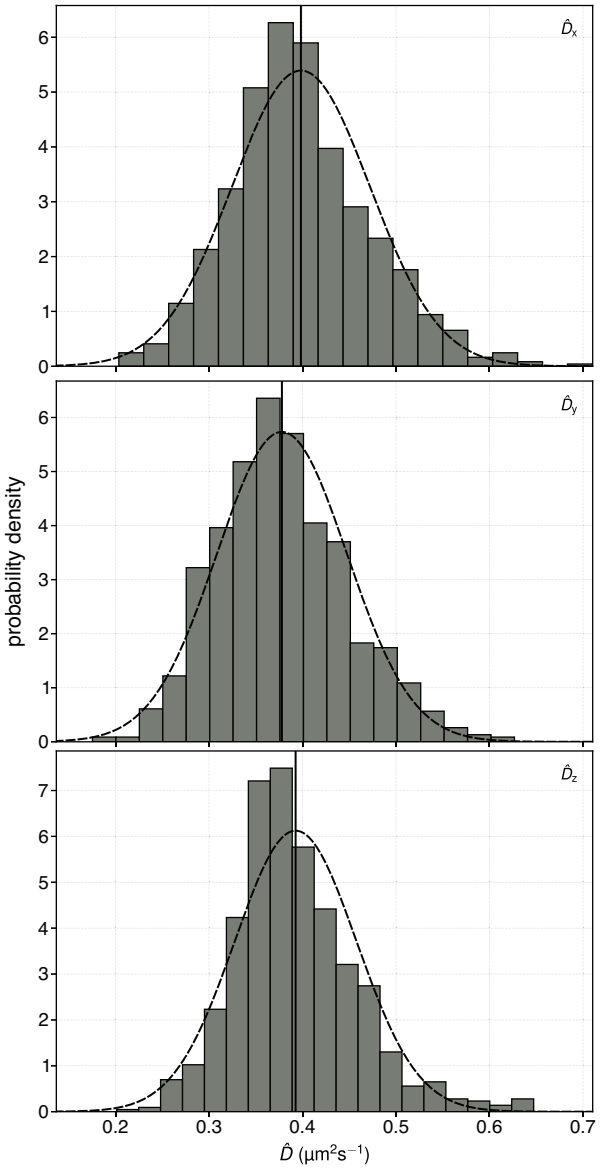

Figure S8: Translational diffusion coefficients of the rods measured in 60:40 glycerol:water v/v.

S9 Rotational Diffusion Coefficients

For the extraction of rotational diffusion coefficients, we take the rotational diffusion coefficient to be $1/(6 * \tau_{\text{acf}})$, where τ_{acf} is the lifetime extracted from the autocorrelation function of the polarization contrast fluctuation function. [1] As can be seen, comparison

to the theoretical prediction [15] for the average rod geometry of 78.46 nm × 32.79 nm at 293.15 K is excellent when one considers that the rotational diffusion coefficients from experiment will be slower due to the hydrodynamic radius being slightly in excess of the TEM-defined geometry.

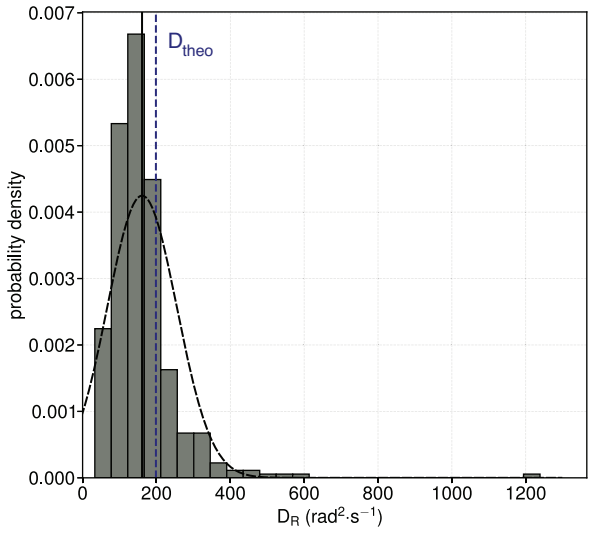

Figure S9: Rotational diffusion coefficients of the rods measured in 60:40 glycerol:water v/v.

S10 Histogram of orientations

Here we show histograms of the angles determined from analysis of the full track from which the data shown in Fig. 4 are taken. As can be seen, both θ and ϕ agree well with the expected distributions of free diffusion.

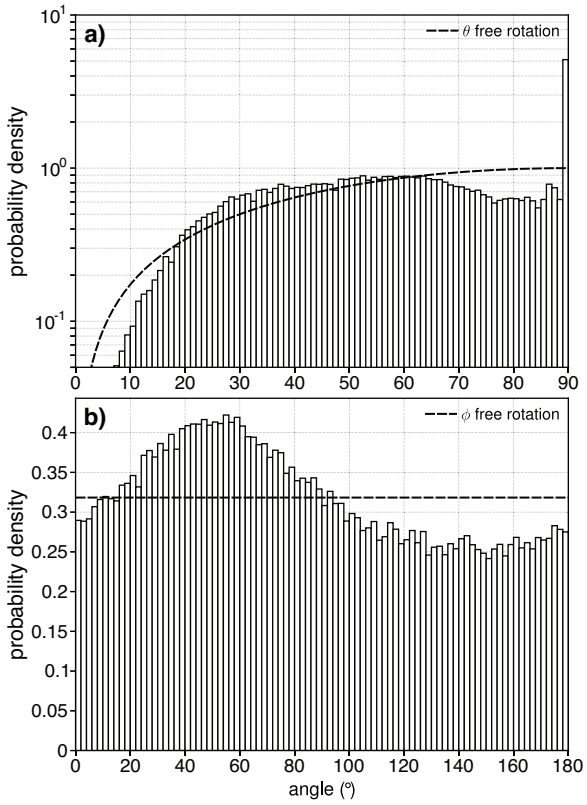

Figure S10: Histograms of a) θ and b) ϕ recovered from the analysis of the full data set shown in Fig. 4, compared to free diffusion models (dashed lines).

S11 Comparison between measured & simulated ϕ jump data

The large displacements in the ϕ coordinate in Fig. 4 are due, essentially, to the periodic nature of the 0 to 180° coordinate we may determine our ϕ angles over. This is shown explicitly in Figure S11, where we first observe that for free diffusion (simulated using the same procedure as described in section S5 but using 250 µs time steps and a 200 $\text{rad}^2 \cdot \text{s}^{-1}$ rotational diffusion coefficient) over a full sphere, these large displacements are not observed. When the same data is "coerced" (as it would be in experiment) to the quarter-sphere, these larger displacements appear. To provide further clarity, we plot the ϕ steps from experiment (Fig. S11 c) and from the simulation across a quarter sphere in (Fig. S11 d). As can be seen, the distributions are qualitatively similar, implying that the large displacements observed in the real data are simply a result of the fact that the experiment may only determine the orientation to a single quarter-sphere. That there is a minor difference is likely the result of the simplified model of rotational diffusion, which assumes that the diffuser is spherical. The agreement in shape clearly shows that the large displacements are likely due to the periodicity of the coordinates, however.

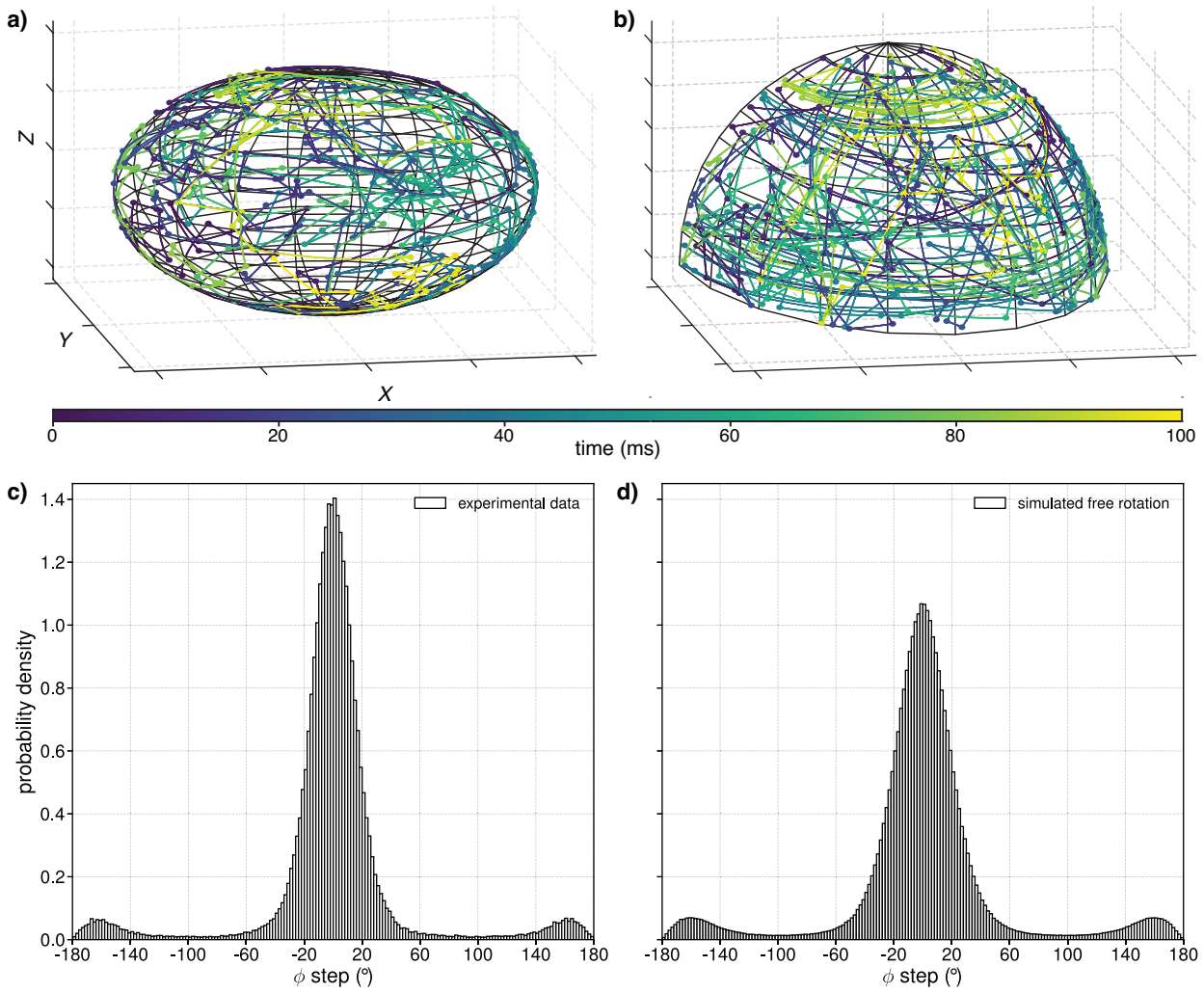

Figure S11: a) Full sphere of simulated rotational diffusion for 100 ms. b) Same as in a) but coerced to a quarter-sphere as is done in experiment by the $D_{\infty h}$ symmetry. c) ϕ steps from experimental data (from the data set of which 100 ms is shown in Fig. 4), d) ϕ steps from full 2×10^6 step simulated data trace of which 100 ms is shown in a) and b).

S12 Description of supplementary videos

jp1c08917_si_002.flv shows the translation of the rod over the full 34 s track, as well as the rotation (shown as a black bar) over this time. Each frame corresponds to 20 ms and the video plays at 20 fps.

jp1c08917_si_003.flv shows the rotation of the rod in a quarter-sphere over 200 ms. Each frame is 250 μs and the video plays at 20 fps.

References

(1) Guerra, L. F.; Muir, T. W.; Yang, H. Single-Particle Dynamic Light Scattering: Shapes of Individual Nanoparticles. *Nano Lett.* **2019**, *19*, 5530–5536.

(2) Fourkas, J. T. Rapid Determination of the Three-Dimensional Orientation of Single Molecules. *Opt. Lett.* **2001**, *26*, 211–213.

(3) Yang, H. Single-Particle Light Scattering: Imaging and Dynamical Fluctuations in the Polarization and Spectral Response. *J. Phys. Chem. A* **2007**, *111*, 4987–4997.

(4) Cang, H.; Wong, C. M.; Xu, C. S.; Rizvi, A. H.; Yang, H. Confocal Three Dimensional Tracking of a Single Nanoparticle with Concurrent Spectroscopic Readouts. *Appl. Phys. Lett.* **2006**, *88*, 223901.

(5) Welsher, K.; Yang, H. Imaging the Behavior of Molecules in Biological Systems: Breaking the 3D Speed Barrier with 3D Multi-Resolution Microscopy. *Faraday Discuss.* **2015**, *184*, 359–379.

(6) Xu, C. S.; Cang, H.; Montiel, D.; Yang, H. Rapid and Quantitative Sizing of Nanoparticles Using Three-Dimensional Single-Particle Tracking. *J. Phys. Chem. C* **2007**, *111*, 32–35.

(7) Enderlein, J.; Toprak, E.; Selvin, P. R. Polarization Effect on Position Accuracy of Fluorophore Localization. *Opt. Express* **2006**, *14*, 8111–8120.

(8) Byron, M. L.; Variano, E. A. Refractive-Index-Matched Hydrogel Materials for Measuring Flow-Structure Interactions. *Exp Fluids* **2013**, *54*, 1456.

(9) Hunter, G. L.; Edmond, K. V.; Elsesser, M. T.; Weeks, E. R. Tracking Rotational Diffusion of Colloidal Clusters. *Opt. Express* **2011**, *19*, 17189–17202.

(10) Watkins, L. P.; Yang, H. Detection of Intensity Change Points in Time-Resolved Single-Molecule Measurements. *J. Phys. Chem. B* **2005**, *109*, 617–628.

(11) Guerra, L. F.; Muir, T. W.; Yang, H. Determining the Spheroid Geometry of Individual Metallic Nanoparticles by Two-Dimensional Single-Particle Dynamic Light Scattering. *J. Phys. Chem. C* **2019**, *123*, 18565–18572.

(12) Lu, C.-Y.; Vanden Bout, D. A. Analysis of Orientational Dynamics of Single Fluorophore Trajectories from Three-Angle Polarization Experiments. *J. Chem. Phys.* **2008**, *128*, 244501.

(13) Hanson, J. A.; Yang, H. A General Statistical Test for Correlations in a Finite-Length Time Series. *J. Chem. Phys.* **2008**, *128*, 214101.

(14) Montiel, D.; Cang, H.; Yang, H. Quantitative Characterization of Changes in Dynamical Behavior for Single-Particle Tracking Studies. *J. Phys. Chem. B* **2006**, *110*, 19763–19770.

(15) Tirado, M. M.; Martínez, C. L.; de la Torre, J. G. Comparison of Theories for the Translational and Rotational Diffusion Coefficients of Rod-like Macromolecules. Application to Short DNA Fragments. *J. Chem. Phys.* **1984**, *81*, 2047–2052.